



Prediction of Thermal Behavior in Ferromagnetic Carreau Fluids Using Neural Networks Algorithm

Saraj Khan¹, Muhammad Imran Asjad^{1,2,*}, Muhammad Naeem Aslam³,
Marei S. Alqarni⁴, Liliana Guran⁵

¹ *Department of Mathematics, University of Management and Technology, Lahore 54770, Pakistan*

² *Jadara University Research Center, Jadara University, Irbid, Jordan*

³ *Department of Mathematics, Lahore Garrison University, Lahore, Pakistan*

⁴ *Department of Mathematics, College of Science, King Khalid University, Abha 61413, Saudi Arabia*

⁵ *Department of Hospitality Services, Faculty of Business, Babes-Bolyai University, Horea Street No. 7, 400174, Cluj-Napoca, Romania*

Abstract. This study investigates the melting heat transfer characteristics of a ferromagnetic Carreau fluid (FCF) influenced by an external magnetic dipole. The Carreau model captures the non-Newtonian shear-thinning and shear-thickening nature of the fluid, while ferromagnetic effects introduce magnetically induced forces that modify flow and heat transport. The governing nonlinear ordinary differential equations are solved using MATLAB's `bvp4c` solver. The resulting reference data are used to train an Artificial Neural Network (ANN) optimized via the Levenberg–Marquardt Technique (LMT). The proposed ANN–LMT framework demonstrates high predictive accuracy with low Mean Squared Error (MSE) values, showing excellent agreement with numerical results. A specific set of physical parameters including the melting parameter (B), ferromagnetic interaction parameter (β), Eckert number (Ec), Prandtl number (Pr), Schmidt number (Sc), dimensionless Curie temperature (ϵ) and Weissenberg number (We) was used to simulate the ferromagnetic Carreau fluid flow. Physically, increasing We and β reduces the velocity, while higher Pr and B suppress temperature and concentration due to diffusion and melting effects. Conversely, greater Ec enhances thermal gradients, Sc weakens solute diffusion, and rising ϵ increases concentration. Overall, the ANN–LMT model provides an efficient and accurate computational alternative for analyzing complex magnetothermal flow systems, with potential extensions to unsteady and three-dimensional configurations.

2020 Mathematics Subject Classifications: 76W05, 80A20, 68T07, 76A05

Key Words and Phrases: Levenberg–Marquardt algorithm, ferromagnetic Carreau fluid, thermal boundary layer, thermal behavior prediction, magnetohydrodynamics

*Corresponding author.

DOI: <https://doi.org/10.29020/nybg.ejpam.v18i4.6795>

Email addresses: saraj.khan.niazi@gmail.com (S. Khan),
imran.asjad@umt.edu.pk (M. I. Asjad), muhammadnaeemaslam10@gmail.com (M. N. Aslam),
msalqarni@kku.edu.sa (M. S. Alqarni), liliana.guran@ubbcluj.ro (L. Guran)

1. Introduction

Ferromagnetic Carreau fluids form a unique class of complex fluids that combine shear dependent viscosity with magnetic responsiveness, enabling control through external magnetic fields [1–3]. This dual behavior, arising from the Carreau model's non-Newtonian rheology and magnetic susceptibility, has made such fluids valuable in applications like magnetic drug delivery, ferrofluid-based heat exchangers, microfluidics, and cooling systems [4]. The interaction between magnetic forces and nonlinear viscosity introduces additional complexity in flow modeling and heat transfer analysis. Shah et al. [5] examined MHD convective heat transfer in Carreau fluids and found that temperature-dependent viscosity and conductivity significantly affect the thermal boundary layer, while Al-Khafajy et al. [6] analyzed peristaltic transport in elastic channels, revealing key insights into non-Newtonian flow behavior under physiological conditions.

Rehman et al. [7] analyzed thermal behavior in converging channels with mass transfer and Cattaneo-Christov heat flux, highlighting the critical role of inertia and heat propagation delays in flow modulation. Kutev et al. [8] provided a theoretical investigation into unsteady Carreau fluid flow in pipes, identifying bounds on flow behavior through rheological parameters. Ghosh et al. [9] obtained analytical solutions for ferrofluid convection influenced by a transverse magnetic field, offering a clearer understanding of magnetic damping in boundary layers. Al-Obaidi et al. [10] examined the magnetic stabilization of flow in porous media, indicating that magnetic field strength plays a critical role in flow stability, especially when the Grashof number is significant. The importance of magnetic dipole effects has also been explored in biofluid and non-Newtonian flow models. Dharmiah et al. [11] investigated radiative MHD blood flow under the influence of a magnetic dipole, incorporating Brownian motion and thermophoresis. Their results emphasized the significance of magnetic body forces in controlling temperature and velocity profiles in physiological environments.

Heat transfer is a critical aspect in ferromagnetic Carreau fluid, as thermal energy governs both phase transitions and the fluid's magnetic response. Hobiny et al. [12] numerically examined viscous dissipation in Carreau fluids, pointing out how shear-dependent viscosity affects thermal energy conversion. In advanced energy systems, Bilal et al. [13] used the parametric continuation method to model energy transfer in Carreau-Yasuda fluids with magnetic dipoles and hybrid nanoparticles. Their study demonstrated that ternary hybrid nanofluids outperform simpler fluids in thermal enhancement. Further, magnetized Carreau fluid is sensitive to mass transfer processes. Diffusion and convection influence the dispersion of magnetic particles, affecting the overall concentration field and functionality of the fluid. Thirupathi et al. [14] modeled stagnation point flow of a Carreau nanofluid under MHD effects, showing how magnetic and viscous forces reshape flow dynamics. Asha et al. [15] applied the multi-step differential transformation method to examine Joule heating in peristaltic Carreau nanoflows, while Rooman et al. [16] investigated heat transfer and solute transport in renal flow channels using a Carreau model, emphasizing biomedical relevance.

The Levenberg–Marquardt technique is a widely recognized optimization method that

plays a crucial role in neural network training, particularly for nonlinear regression and curve-fitting tasks. This technique was originally introduced by Kenneth Levenberg in 1944 [17] as a way to solve nonlinear least-squares problems by blending the principles of gradient descent and the Gauss–Newton method. His approach introduced a damping factor to stabilize convergence, which proved particularly effective when the Gauss–Newton method struggled near saddle points or ill-conditioned regions. In 1963, Donald Marquardt refined the method [18], improving its stability and performance for estimating parameters in complex nonlinear systems. This combined approach, now referred to as the Levenberg–Marquardt algorithm, provides an effective interpolation between the robustness of gradient descent and the fast convergence of Gauss–Newton.

Hagan et al. [19] highlighted the efficiency of the Levenberg–Marquardt technique in training feedforward neural networks, offering fast convergence and high accuracy for medium-sized datasets. Moré [20] noted its robustness in handling complex, ill-conditioned error surfaces, while Huang and Loh [21] demonstrated its strength in nonlinear system modeling. Building on these advantages, recent works have applied LMT-based neural networks to nonlinear fluid dynamics. Albasheir et al. [22] modeled Carreau nanofluid stagnation flow under magnetic and heat generation effects, achieving improved prediction of thermal and solutal gradients. Similar studies on MHD Carreau fluid flows with slip and heat generation confirmed the method’s precision in capturing nonlinear transport behavior [23–26].

Machine learning has become a powerful approach for modeling and optimizing complex transport phenomena in non-Newtonian and nanofluid flows. Abbasi et al. [27] used an ML-based framework to predict the 3D behavior of Carreau fluids under Cattaneo–Christov double diffusion theory, while Alhamdi et al. [28] applied supervised learning to enhance heat transfer in bio-convective Carreau blood-based nanofluid flow with nonlinear radiation [29, 30]. Priyadharshini et al. [31, 32] optimized ternary hybrid nanofluid and MHD flow using machine learning and gradient descent regression, and Kumar et al. [33, 34] employed deep neural networks and SVMs to predict and classify tri-hybrid nanofluid heat transfer. Baithalu et al. [35] further used a Levenberg–Marquardt neural approach for micropolar nanofluid transport with Cattaneo–Christov flux, emphasizing AI’s growing impact on accurate and efficient thermal-fluid modeling. Ayub et al. [36] developed a neural intelligent model to study heat transfer in tri-hybrid cross bio-nanofluid flow over a wedge, showing high accuracy in predicting nonlinear thermal behavior.

Asghar et al. [37] applied an ANN approach to solve a nonlinear Cassava mosaic disease model, demonstrating the robustness of ANN techniques in capturing complex biological dynamics. Hassan et al. [38] investigated heat transfer and entropy generation in ferrofluids under a low oscillating magnetic field and reported significant effects of magnetic oscillations on thermal irreversibility. Rizwan et al. [39] developed a rheological model for metallic oxide nanoparticles dispersed in non-Newtonian nanofluids and explored their heat and mass transfer characteristics, revealing enhanced thermal performance due to nanoparticle interactions and flow behavior. Arif et al. [40] investigated cross-diffusion in MHD Williamson nanofluid flow over a nonlinear stretching surface using Morlet wavelet neural networks, demonstrating the method’s accuracy in capturing nonlinear thermal and

concentration effects. Alraddadi et al. [41] analyzed a ternary hybrid cross bio-nanofluid in an expanding/contracting cylinder under an inclined magnetic field, showing improved heat transfer. Shah et al. [42] proposed an efficient numerical scheme for melting energy transport in time-dependent Carreau nanofluids. Shah et al. [43] further examined inclined MHD tri-hybrid bio-nanofluid flow using an ANN approach.

Despite extensive research on non-Newtonian fluids and magnetohydrodynamic (MHD) effects, limited attention has been paid to the integration of ferromagnetic behavior with phase change phenomena in Carreau-type fluids. Additionally, few studies have addressed the computational challenges of solving such highly nonlinear boundary layer problems using intelligent data-driven strategies. Motivated by this gap, the present work explores the melting heat transfer characteristics of ferromagnetic Carreau fluid (FCF) under the influence of a magnetic dipole field. A novel hybrid methodology is proposed that combines the traditional `bvp4c` numerical scheme with the Levenberg–Marquardt backpropagation technique (LMT), enabling accurate approximation of velocity, temperature, and concentration profiles. The application of LMT to this class of FCF problems introduces a robust predictive framework, offering enhanced accuracy, faster convergence, and deeper insight into the coupled thermal–solutal behavior of magnetized non-Newtonian systems.

The primary objective of this study is to develop an efficient and accurate computational framework for analyzing the melting heat transfer and flow characteristics of a FCF under the influence of an external magnetic dipole. To achieve this, the nonlinear boundary value problem governing the FCF is formulated and solved using MATLAB's `bvp4c` solver to obtain reliable reference data for velocity, temperature, and concentration profiles. An artificial neural network trained with the LMT is then employed to approximate these reference solutions and evaluate the model's predictive accuracy. The ANN–LMT predictions are compared with the numerical results to validate the robustness, convergence, and generalization capability of the proposed hybrid modeling approach. This methodology effectively bridges numerical precision and data-driven learning, offering a reliable framework for simulating nonlinear magnetothermal systems influenced by melting and diffusion effects.

The present study is guided by several research questions that define its scope and objectives. It investigates how effectively a supervised neural network optimized with the Levenberg–Marquardt algorithm can predict the nonlinear thermal and flow behavior of ferromagnetic Carreau fluids. It also explores the combined effects of magnetic interaction, Weissenberg number, and Prandtl number on the velocity and temperature profiles of such fluids. Finally, it examines how accurately the proposed ANN–LMT framework can reproduce the results obtained from conventional numerical solvers such as MATLAB's `bvp4c`.

The structure of the paper is outlined as follows: Section 1 presents a detailed review of the relevant literature along with the physical context underlying the study. Section 2 formulates the mathematical model by introducing the governing equations and corresponding boundary conditions. In Section 3, the implementation of an ANN–LMT for modeling the ferromagnetic Carreau fluid is discussed. Section 4 provides graphical results and a comprehensive discussion of the observed physical behavior. Finally, Section 5

summarizes the main conclusions of the study.

2. Problem Modeling

Figure 1 shows the two-dimensional flow of a ferromagnetic nanofluid over an impermeable sheet of a stretched sheet horizontally. A magnetic field is applied on the outside to affect the flow. The x-axis has two equal and opposite forces, and the y-axis is perpendicular to the surface of a sheet. The sheet is above a fixed distance of a y-axis by a magnetic dipole of known strength with a fixed field in the positive x-direction. This generates a magnetic field owing to the dipole; this boosts the magnetic field concentration locally, and ultimately the magnetic field effects lead to magnetic saturation in the ferrofluid.

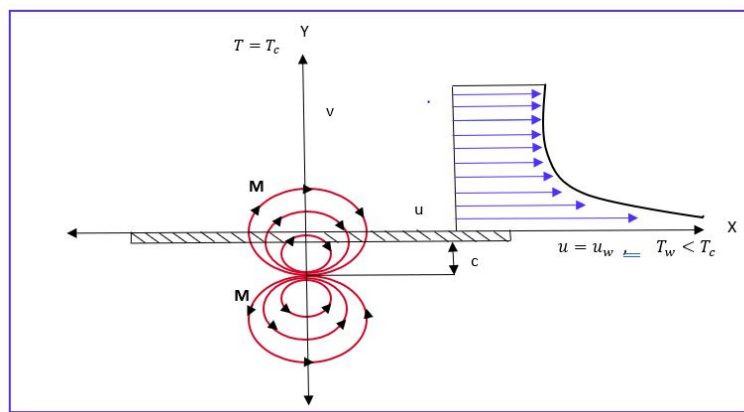


Figure 1: Flow geometry

The temperature of the sheet, which we indicate by T_w , is kept below the Curie temperature T_c . At temperatures beyond this magnetization limit, the ferromagnetic nanoparticles lose their magnetism and end up becoming paramagnetic particles. It is assumed that the fluid far from the sheet has a temperature $T_\infty = T_c$, meaning the nanoparticles remain non-magnetic until they cool upon entering the thermal boundary layer. A mathematical model is formulated to examine the influence of magnetic dipoles on a generalized Newtonian (Carreau) nanofluid, incorporating the effects of viscous dissipation and chemical reactions.

The governing equations describing the conservation of mass, momentum, energy, and concentration for a two-dimensional, incompressible, steady flow of a ferromagnetic Carreau fluid are first expressed in their general vector form as follows [44]:

$$\begin{aligned}\nabla \cdot \mathbf{V} &= 0, \\ \rho(\mathbf{V} \cdot \nabla)\mathbf{V} &= -\nabla p + \nabla \cdot \boldsymbol{\tau} + \mathbf{F}_m, \\ \rho c_p(\mathbf{V} \cdot \nabla T) &= k \nabla^2 T + Q_T,\end{aligned}$$

$$(\mathbf{V} \cdot \nabla C) = D_B \nabla^2 C + \frac{D_T}{T_c} \nabla^2 T.$$

Here, $\mathbf{V} = (\bar{u}, \bar{v})$ denotes the velocity vector, ρ is the fluid density, p is the pressure, T represents the temperature, and C denotes the nanoparticle concentration. The extra stress tensor $\boldsymbol{\tau}$ for the Carreau fluid model is defined as

$$\boldsymbol{\tau} = 2 \mu_{\text{eff}}(\dot{\gamma}) \mathbf{D}, \quad \mathbf{D} = \frac{1}{2} (\nabla \mathbf{V} + (\nabla \mathbf{V})^T),$$

where \mathbf{D} is the rate of deformation tensor and $\mu_{\text{eff}}(\dot{\gamma})$ is the effective viscosity given by the Carreau relation,

$$\mu_{\text{eff}}(\dot{\gamma}) = \mu \left[1 + (\Gamma \dot{\gamma})^2 \right]^{\frac{n-1}{2}},$$

with $\dot{\gamma} = \sqrt{2 \mathbf{D} : \mathbf{D}}$ being the shear rate.

The magnetic body force \mathbf{F}_m arises due to the spatial variation of magnetization and magnetic field intensity, and for a temperature-dependent magnetization $M(T)$, it is expressed as

$$\mathbf{F}_m = \mu_0 M(T) \nabla H,$$

where μ_0 denotes the magnetic permeability, $M(T)$ is the magnetization, and H represents the magnetic field strength.

The term Q_T in the energy equation accounts for the thermal effects induced by magnetization and can be written as

$$Q_T = \mu_0 T \frac{dM}{dT} (\mathbf{V} \cdot \nabla H),$$

which incorporates the coupling between the temperature gradient, magnetization, and the applied magnetic field.

The last equation represents the nanoparticle concentration field, which includes both Brownian motion and thermophoretic diffusion effects through the coefficients D_B and D_T , respectively.

The above vector equations can be expressed explicitly in their two-dimensional component form as:

$$\frac{\partial \bar{v}}{\partial y} + \frac{\partial \bar{u}}{\partial x} = 0, \quad (1)$$

$$\frac{\partial \bar{u}}{\partial y} \bar{v} + \frac{\partial \bar{u}}{\partial x} \bar{u} = -\frac{1}{\rho} \frac{\partial p}{\partial x} + \frac{3\nu(n-1)}{2} \Gamma \left(\frac{\partial \bar{u}}{\partial y} \right)^2 \frac{\partial^2 \bar{u}}{\partial y^2} + \frac{\mu_0 M}{\rho} \frac{\partial H}{\partial x}, \quad (2)$$

$$\frac{\partial T}{\partial y} \bar{v} + \frac{\partial T}{\partial x} \bar{u} + \frac{\mu_0}{\rho c_p} T \frac{\partial M}{\partial T} \left(\bar{u} \frac{\partial H}{\partial x} + \bar{v} \frac{\partial H}{\partial y} \right) = \frac{k}{\rho c_p} \frac{\partial^2 T}{\partial y^2}, \quad (3)$$

$$\frac{\partial C}{\partial x} \bar{u} + \frac{\partial C}{\partial y} \bar{v} = \frac{D_T}{T_c} \frac{\partial^2 T}{\partial y^2} + D_B \frac{\partial^2 C}{\partial y^2}. \quad (4)$$

The boundary conditions suitable for solving the governing equations are expressed as follows:

$$\begin{cases} y = 0: & \bar{v} = 0, \quad \bar{u} = u_w = ax, \quad k \left(\frac{\partial T}{\partial y} \right) = \rho \bar{v}(0) [C_s(T_w - T_0) + \lambda_1], \quad C = C_w = C_c - \frac{B_1 x}{L}, \quad T = T_w, \\ y \rightarrow \infty: & \bar{v} = 0, \quad \bar{u} \rightarrow 0, \quad T \rightarrow T_c, \quad C \rightarrow C_\infty = C_c - \frac{D_1 x}{L}. \end{cases} \quad (5)$$

It is worth noting that the melting boundary condition in Eq. 5 unifies the effects of heat flux and melting within a single formulation. This treatment is based on the interfacial energy balance principle, wherein the latent heat absorbed at the solid–liquid interface is directly related to the temperature difference across the boundary. The present boundary expression is consistent with the formulation described by Endalew and Sarkar [44], ensuring that the thermal energy absorbed due to melting is properly coupled with conductive heat transfer at the surface.

The parameters that are used in the governing equations are λ_1 as the latent heat of the nanofluid, T_0 as the temperature of the solid surface, and C_s as the heat capacity of the solid surface. The model parameters, B_1 and D_1 , are both positive constants, whereas the characteristic length scale is $L = \sqrt{\nu/a}$, where a is a stretching rate constant and ν is the kinematic viscosity.

The effect of the magnetic field on the FCF flow is presented with the help of the magnetic dipole. The magnetic scalar potential that corresponds to this dipole can be written as [45]:

$$\Phi = \frac{\alpha_1}{2\pi} \left(\frac{x}{x^2 + (y + \bar{c}_1)^2} \right). \quad (6)$$

The parameter α_1 is magnetic field strength at the source, and components of a magnetic field vector H are denoted as follows:

$$H_x = \frac{\partial \Phi}{\partial x} = \frac{\alpha_1}{2\pi} \left[\frac{x^2 - (y + \bar{c}_1)^2}{(x^2 + (y + \bar{c}_1)^2)^2} \right] \quad (7)$$

$$H_y = \frac{\partial \Phi}{\partial y} = \frac{\alpha_1}{2\pi} \left[\frac{2x(y + \bar{c}_1)}{(x^2 + (y + \bar{c}_1)^2)^2} \right] \quad (8)$$

The magnetic body force being proportional to the gradient of the magnetic field magnitude H , it is necessary that:

$$H = \left[\left(\frac{\partial \Phi}{\partial x} \right)^2 + \left(\frac{\partial \Phi}{\partial y} \right)^2 \right]^{1/2}, \quad (9)$$

$$\frac{\partial H}{\partial x} = \frac{\alpha_1}{2\pi} \left(\frac{2x}{(y + \bar{c}_1)^4} \right), \quad \frac{\partial H}{\partial y} = \frac{\alpha_1}{2\pi} \left(-\frac{2}{(y + \bar{c}_1)^3} + \frac{4x^2}{(y + \bar{c}_1)^5} \right). \quad (10)$$

An approximate linear relation is employed to express the dependence of magnetization M on temperature T as:

$$M = -K(T - T_c) \quad (11)$$

A parameter known as the pyromagnetic coefficient is indicated by the symbol K . For ferrohydrodynamic interaction to occur, two essential conditions must be satisfied: (i) the fluid temperature T must remain below the Curie temperature T_c , that is, $T_c > T$; and (ii) a nonhomogeneous magnetic field must be applied. Ferrofluid must be heated up to its Curie temperature T_c to guarantee that no more magnetization will occur. At a temperature of this, the ferrofluid will stay closer to the surface, as seen through equation (11).

The equations that govern the FCF flow model are also non-dimensionalized by introducing the following dimensionless quantities:

$$\begin{cases} \psi(\eta) = x\sqrt{\nu a}f, & \eta = \sqrt{\frac{a}{\nu}}y, \\ u = \frac{\partial \psi}{\partial y}, & v = -\frac{\partial \psi}{\partial x}, \\ \theta(\eta) = \frac{T_c - T}{T_c - T_w}, & \phi(\eta) = \frac{C_c - C}{C_c - C_w} \end{cases} \quad (12)$$

The use of the previously defined stream function automatically satisfies the continuity equation (1). By employing an appropriate similarity transformation, the partial differential equations (2)–(4) are reduced to a system of highly nonlinear and coupled ODEs.

$$\left(1 + \frac{3(n-1)}{2} \text{We}^2 f'^2 \right) f''' - f'^2 + f f'' - \frac{2\beta\theta}{(\eta + \alpha)^4}, \quad (13)$$

$$\theta'' + \text{Pr}(f\theta' - f'\theta) - \text{Pr Ec} \beta(\theta - \epsilon) \left(\frac{2f'}{(\eta + \alpha)^4} + \frac{4f}{(\eta + \alpha)^5} \right) + \lambda\beta(\theta - \epsilon) \frac{2f}{(\eta + \alpha)^3} = 0 \quad (14)$$

$$\phi'' + \text{Sc}(f\phi' - f'\phi) = 0 \quad (15)$$

The resulting boundary conditions, which were obtained using the similarity transformation, are as given below:

$$\begin{cases} f'(0) = 1, & \theta(0) = 1, & B\theta'(0) + \text{Pr}f(0) = 0, & \phi(0) = 1, \\ f'(\infty) = 0, & \theta(\infty) = 0, & \phi(\infty) = 0. \end{cases} \quad (16)$$

The physical parameters describing the flow are the following:

$$\begin{cases} \text{Pr} = \frac{\rho c_p}{\nu k}, & \beta = \frac{\mu_0 K \rho \alpha_1 (T_c - T_w)}{2\pi \mu^2}, & \lambda = \frac{\mu^2 a}{a k_p}, & \alpha = \sqrt{\frac{\bar{c}_1^2 \rho a}{\mu}}, \\ B = \frac{C_p (T_c - T_w)}{C_s (T_0 - T_w) + \lambda_1}, & \text{Ec} = \frac{u_w^2}{c_p (T_c - T_w)}, & \text{Sc} = \frac{\nu}{D}, \\ \text{We} = \Gamma a, & \epsilon = \frac{T_c}{T_c - T_w} \end{cases} \quad (17)$$

The dimensionless parameters used are as follows: Pr the Prandtl number, the ferrohydrodynamic interaction parameter is denoted by β , the viscous dissipation parameter is defined as λ , and the non-dimensional distance between the origin and the center of the magnetic pole is set as α . As well, B is the melting parameter, Ec is the Eckert number, Sc is the Schmidt number, We is the Weissenberg number, and the dimensionless Curie temperature is ϵ .

3. Artificial Neural Network Modeling of FCF using LMT

A feedforward artificial neural network (ANN) is employed to approximate the nonlinear behavior of ferromagnetic Carreau fluid (FCF), trained using the Levenberg–Marquardt technique (LMT). This hybrid approach combines the rapid convergence of the Gauss–Newton method with the robustness of gradient descent, offering an efficient framework for solving the governing differential equations.

The LMT algorithm utilizes a damped least-squares optimization scheme. The weights \mathbf{w} are updated iteratively as:

$$\mathbf{w}_{k+1} = \mathbf{w}_k - \left(\mathbf{J}^\top \mathbf{J} + \mu \mathbf{I} \right)^{-1} \mathbf{J}^\top \mathbf{e},$$

where:

- The Jacobian matrix of partial derivatives of network error with respect to weights is denoted as \mathbf{J} ,

- \mathbf{e} is the error vector between predicted and target outputs,
- μ is the damping factor,
- \mathbf{I} is the identity matrix.

The term $\mathbf{J}^\top \mathbf{J}$ approximates the Hessian matrix, while $\mathbf{J}^\top \mathbf{e}$ represents the gradient. This formulation ensures stable and accurate training of the ANN for capturing the flow behavior under complex physical conditions.

In this study, the input features include spatial variables and physical parameters such as B , β , Ec , Pr , Sc , ϵ , and We , while the target outputs are velocity, temperature, and concentration values obtained using MATLAB's `bvp4c` solver. These datasets are then fed into a supervised neural network with the following configuration:

- **Architecture:** One hidden layer with 10 neurons.
- **Activation:** The hidden layer uses the `tanh` (hyperbolic tangent sigmoid) activation function, suitable for smooth approximation of nonlinear mappings.
- **Training Algorithm:** `trainlm`, MATLAB's implementation of LMT.
- **Data Division:** 70% training, 15% testing and 15% validation.
- **Performance Measure:** Mean squared error (MSE).

The training process is executed using either MATLAB's GUI-based `nftool` Graphical User Interface. This hybrid LMT-ANN approach demonstrates fast convergence and high precision in capturing the complex dynamics of magnetized non-Newtonian flow, as reflected in the convergence metrics and predictive accuracy summarized in Table 1.

4. Graphical Results and Discussion

Table 1: LMT performance metrics for different physical parameters in FCF flow.

Parameter	Label	MSE			Epoch	Elapsed Time	Performance	Gradient	Mu
		Training	Validation	Testing					
B	a	1.44×10^{-8}	1.46×10^{-8}	2.03×10^{-8}	711	03 sec	1.23×10^{-8}	1.00×10^{-7}	1.00×10^{-9}
β	b	2.07×10^{-9}	1.97×10^{-9}	2.57×10^{-9}	763	01 sec	3.11×10^{-9}	9.43×10^{-8}	1.00×10^{-8}
Ec	c	2.17×10^{-8}	3.34×10^{-8}	3.05×10^{-8}	352	01 sec	2.10×10^{-8}	9.98×10^{-8}	1.00×10^{-8}
Pr	d	1.85×10^{-9}	2.10×10^{-9}	3.10×10^{-9}	507	02 sec	2.33×10^{-9}	9.94×10^{-8}	1.00×10^{-7}
We	e	7.21×10^{-9}	9.15×10^{-9}	8.72×10^{-9}	500	02 sec	9.91×10^{-9}	9.96×10^{-8}	1.00×10^{-7}
ϵ	f	1.34×10^{-9}	1.79×10^{-9}	2.16×10^{-9}	585	02 sec	2.00×10^{-9}	9.95×10^{-8}	1.00×10^{-8}
Sc	g	1.52×10^{-9}	1.68×10^{-9}	1.88×10^{-9}	84	01 sec	1.76×10^{-9}	5.97×10^{-7}	1.00×10^{-9}

Table 1 compiles the convergence outcomes of the Levenberg-Marquardt technique, including mean squared error (MSE) for training, validation, and testing phases, number of

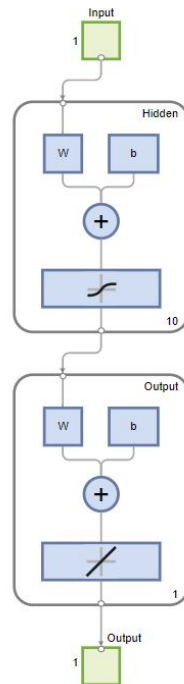


Figure 2: Architecture of the neural network model trained using the LMT for FCF flow.

epochs, elapsed training time, gradient values, and the backpropagation control parameter μ . These results confirm the accuracy and reliability of the LMT-based neural network model across various physical parameters. The LMT is employed to iteratively adjust the network weights, effectively minimizing prediction errors and ensuring high accuracy. Figure 2 presents the neural network architecture and outlines the core mechanism of the Levenberg–Marquardt training process.

The architecture of a feedforward neural network trained using the Levenberg–Marquardt technique is illustrated in Figure 3. The input layer consists of three neurons, denoted as x_1 , x_2 , and x_3 , which represent the input features of the system. These input neurons are fully connected to a single hidden layer comprising ten neurons, labeled as h_1, h_2, \dots, h_{10} . Each hidden neuron employs the tanh activation function, enabling nonlinear transformations of the inputs to enhance the network’s learning capability. The output layer contains a single neuron, labeled y , which produces the final output of the network. All inter-layer connections are fully weighted and adjusted during training using the LMT, a widely used optimization method for training small- to medium-sized neural networks.

Figure 4 presents the flow diagram of the ferromagnetic Carreau fluid (FCF) model along with the integrated Levenberg–Marquardt training procedure. The diagram outlines the interaction between flow, thermal, and concentration fields under the influence of magnetic forces and melting effects. It also demonstrates the use of numerical data from the **bvp4c** solver to train the neural network, where the LMT algorithm iteratively updates weights to minimize prediction errors and enhance learning efficiency.

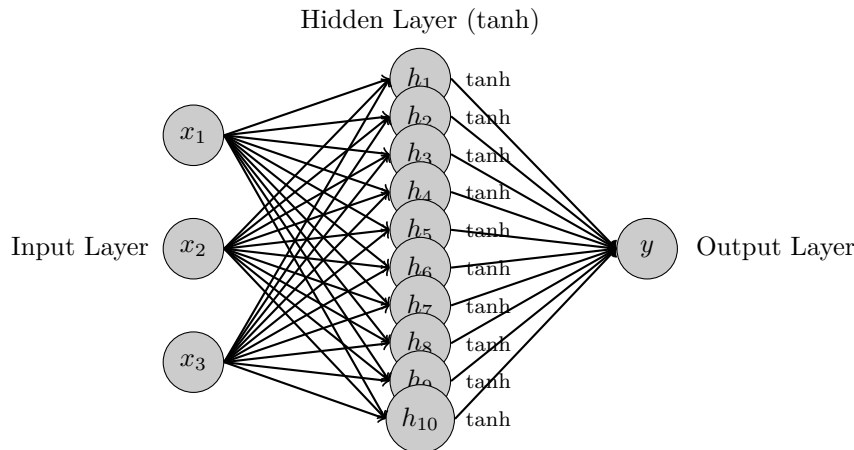


Figure 3: Feedforward neural network structure trained using the LMT.

This study employs the Levenberg-Marquardt technique (LMT) to model the melting heat transfer and flow behavior of a ferromagnetic Carreau fluid subjected to an external magnetic dipole. The governing boundary layer equations, described in Eqs. 13–16, account for the shear-dependent viscosity of the Carreau model and the magnetic body forces due to ferromagnetic properties. MATLAB's **bvp4c** numerical solver provides benchmark solutions against which the neural network results are compared. The input domain is defined as $\eta \in [0, 4]$, discretized into 801 points using a step size of 0.005. For each discretized point, the dependent variables include the velocity $f(\eta)$, temperature $\theta(\eta)$, and concentration $\phi(\eta)$, obtained through the numerical solutions of the governing equations. The reference dataset generated using MATLAB's **bvp4c** solver therefore comprised 801 data samples for each of the seven governing parameters ($B, \beta, Ec, Pr, Sc, \varepsilon, We$), resulting in a total of $(801 \times 7) = 5607$ input–output pairs. Each data instance contained seven input features and three corresponding target variables representing the velocity, temperature, and concentration profiles. The dataset was divided into 70% for training, 15% for validation, and 15% for testing to ensure robust generalization. The reported Mean Squared Error (MSE) values in Table 1 correspond to the testing phase, reflecting the unbiased predictive accuracy of the Levenberg–Marquardt neural network model.

The tuples of the artificial neural network are fed through three layers, where the single hidden layer employs the hyperbolic tangent activation function, commonly referred to as \tanh . The activation function is defined as

$$\tanh(x) = \frac{e^x - e^{-x}}{e^x + e^{-x}} = \frac{2}{1 + e^{-2x}} - 1, \quad (18)$$

which is a smooth and differentiable function that maps real-valued inputs to the range $(-1, 1)$. The \tanh function is particularly suitable for nonlinear regression and function approximation problems because of its symmetry around zero and its ability to capture smooth nonlinear transitions. This symmetric range keeps neuron activations centered near zero, reducing bias shifts and improving gradient flow during backpropagation. As a result, the training process achieves faster convergence and avoids gradient saturation

issues that often occur with other sigmoidal functions. The smooth differentiability of the \tanh function also enhances the network's capacity to learn complex nonlinear dependencies between the physical parameters and the corresponding velocity, temperature, and concentration profiles, thereby improving the predictive accuracy of the model.

Figures 5, 6, and 7 indicate the LMT-based data analysis for the melting parameter (B), the ferromagnetic interaction parameter (β), and the Eckert number (Ec) respectively. Figures 5(a)–11(a) display the LMT validation performance outcomes for the complete dataset under different parametric settings. Figures 5(b)–11(b) illustrate the evolution of the gradient, μ parameter, and validation checks throughout training. Figures 8, 9, 10, and 11 demonstrate the LMT response for the Prandtl number (Pr), the Weissenberg number (We), the Curie temperature (ϵ), and the Schmidt number (Sc) respectively. The corresponding error histograms that reflect the network's prediction accuracy are shown in Figures 5(c)–11(c), revealing that the prediction errors remain closely centered around zero. Regression analysis findings are displayed in Figures 5(d)–11(d), confirming strong correlation between the predicted and target outputs across all settings.

Figures 5(a)–11(a) show the convergence plots of the MSE for the test, training, and validation curves across all parametric settings, indicating that the best performance is achieved at [711, 763, 352, 507, 500, 585, 84] epochs, with MSE values around [1.2347×10^{-8} , 3.1095×10^{-9} , 2.1024×10^{-8} , 2.3325×10^{-9} , 9.9117×10^{-10} , 1.9956×10^{-10} , 1.7624×10^{-9}] respectively. The gradient and μ parameter values for the Levenberg-Marquardt technique are [9.9983×10^{-8} , 9.4343×10^{-8} , 9.9755×10^{-8} , 9.9434×10^{-8} , 9.9612×10^{-8} , 9.947×10^{-8} , 5.9727×10^{-7}] and [1×10^{-9} , 1×10^{-8} , 1×10^{-8} , 1×10^{-7} , 1×10^{-7} , 1×10^{-8} , 1×10^{-9}] respectively, as illustrated in Figures 5(b)–11(b). These results confirm the convergence efficiency and accuracy of the LMT-based neural network approach.

The error histograms in Figures 5(c)–11(c) further corroborate these findings, showing that the difference between network output and reference data remains close to zero. When compared to the reference zero-line error bin, the histograms reveal errors of approximately [-2.1×10^{-5} , 3.54×10^{-6} , 3.91×10^{-5} , 7.53×10^{-6} , 4.11×10^{-6} , -6.1×10^{-7} , -9×10^{-7}] respectively. Figures 5(d)–11(d) illustrate the regression analysis for the ferromagnetic Carreau fluid flow model with melting effects under various parametric configurations. The regression plots reveal strong correlations (R values close to 1), confirming the predictive reliability and accuracy of the neural network trained using the Levenberg-Marquardt technique. Additionally, the limited amount of scatter and the nearly perfect alignment of predicted versus target data suggest the absence of significant errors or missing values in the modeled system. As illustrated in Figures 5(e)–11(e), the fitness graphs throughout the training, validation, and testing phases demonstrate prediction errors in the range of 10^{-5} per unit time. Targets are denoted by dots (\cdot), whereas predicted outcomes for training, validation, and testing are shown by plus signs ($+$).

Figure 12 illustrates the effect of the Weissenberg number (We) on the velocity profile for shear-thinning fluids, characterized by a power-law index $n < 1$. It is evident that the velocity decreases as We increases. The Weissenberg number quantifies the ratio of elastic to viscous effects in a non-Newtonian fluid. An increase in We implies a longer relaxation time, which enhances the elastic response of the fluid. This elevated elasticity

increases the internal resistance to deformation, thereby suppressing the flow and reducing the fluid velocity. The effect is more pronounced in shear-thinning fluids, where viscosity decreases with shear rate, yet elastic stresses continue to resist motion. Figure 13 shows the effect of the ferromagnetic interaction parameter β on the velocity profile. As β increases, the velocity decreases due to the enhanced magnetic field generated by the dipole. This magnetic field introduces a resistive (drag) force that opposes fluid motion, thereby slowing down the flow. The greater the magnetic influence, the stronger the suppression of velocity through magnetically induced resistance.

Figure 14 shows that an increase in the Prandtl number (Pr) reduces the thermal boundary layer thickness for both fluids. Physically, higher Pr indicates lower thermal diffusivity, limiting heat transfer. As a result, the temperature gradient near the surface increases, and the thermal boundary layer becomes thinner than the momentum boundary layer. Figure 15 illustrates the effect of the Weissenberg number (We) on the thermal distribution for both fluid types. For shear-thinning fluids, increasing We enhances the thermal boundary layer thickness due to stronger elastic effects, which promote energy retention. In contrast, shear-thickening fluids show a reduction in thermal boundary layer thickness with higher We , as increased viscosity dominates and restricts thermal diffusion. Figure 16 illustrates the effect of the ferromagnetic interaction parameter β on the temperature profile. This parameter represents the strength of the magnetic field generated by an external dipole. As β increases, the intensified magnetic field imposes a stronger restrictive force on fluid motion, reducing convective mixing and suppressing the fluid's ability to transport thermal energy. As a result, thermal diffusion weakens and the temperature profile decreases for both shear-thinning and shear-thickening fluids. This demonstrates how increased magnetic interaction can inhibit heat transfer by limiting fluid deformation and internal energy distribution.

Melting refers to the phase transition from solid to liquid due to heat absorption. During this process, energy is drawn from the fluid layers adjacent to the surface within the thermal boundary layer. As shown in Figure 17, the inclusion of the melting parameter B reduces the temperature gradient near the wall. This occurs because the heat required for melting lowers the available thermal energy for conduction into the fluid, thereby weakening the thermal boundary layer. Consequently, the surface temperature rises more slowly, and the overall thermal transport is moderated. Figure 18 illustrates the influence of viscous dissipation, represented by the Eckert number (Ec), on the temperature profile. As Ec increases, a noticeable reduction in the thermal boundary layer thickness is observed. Physically, a higher Ec implies more conversion of kinetic energy into internal energy due to viscous effects. However, in this case, the generated heat is localized and does not significantly spread through conduction, resulting in a sharper thermal gradient near the surface and a thinner thermal boundary layer.

Figure 19 presents the effect of the Schmidt number (Sc) on the concentration profile. An increase in Sc indicates a lower mass diffusivity relative to momentum diffusivity, meaning solute particles diffuse more slowly through the fluid. As a result, the concentration boundary layer becomes thinner, and the overall concentration within the fluid decreases. This behavior reflects reduced mass transport due to limited molecular diffu-

sion, especially in fluids with higher viscosity or lower solute mobility. Figure 20 illustrates the effect of the Weissenberg number (We) on the concentration profile. As We increases, the concentration gradient decreases, leading to a lower solute concentration throughout the domain. This behavior is attributed to the increased elastic effects associated with higher We , which enhance fluid resistance and suppress convective transport. Consequently, the reduced mobility of solute particles weakens mass diffusion, resulting in a thinner concentration boundary layer.

The effect of the dimensionless Curie temperature (ϵ) on the concentration profile is presented in Figure 21. The results indicate that the concentration increases with rising ϵ . Physically, an increase in ϵ implies that the system temperature is approaching the Curie temperature, beyond which the ferromagnetic material gradually loses its magnetic properties. As the magnetic field weakens, the associated magnetic body forces that typically aid in the outward diffusion of solute particles diminish. Consequently, the suppression of magnetic convection leads to reduced solute dispersion away from the wall, allowing more solute particles to accumulate in the near-wall region. This results in an enhanced concentration profile within the boundary layer. The effect of the melting parameter B on the concentration profile is illustrated in Figure 22. As B increases, it enhances the heat transfer from the solid surface into the fluid, promoting localized melting and increased thermal energy near the boundary. This elevated thermal activity leads to enhanced mixing and reduces the accumulation of solute near the surface. Consequently, the concentration profile decreases due to the dilution of solute particles and the disruption of the concentration boundary layer.

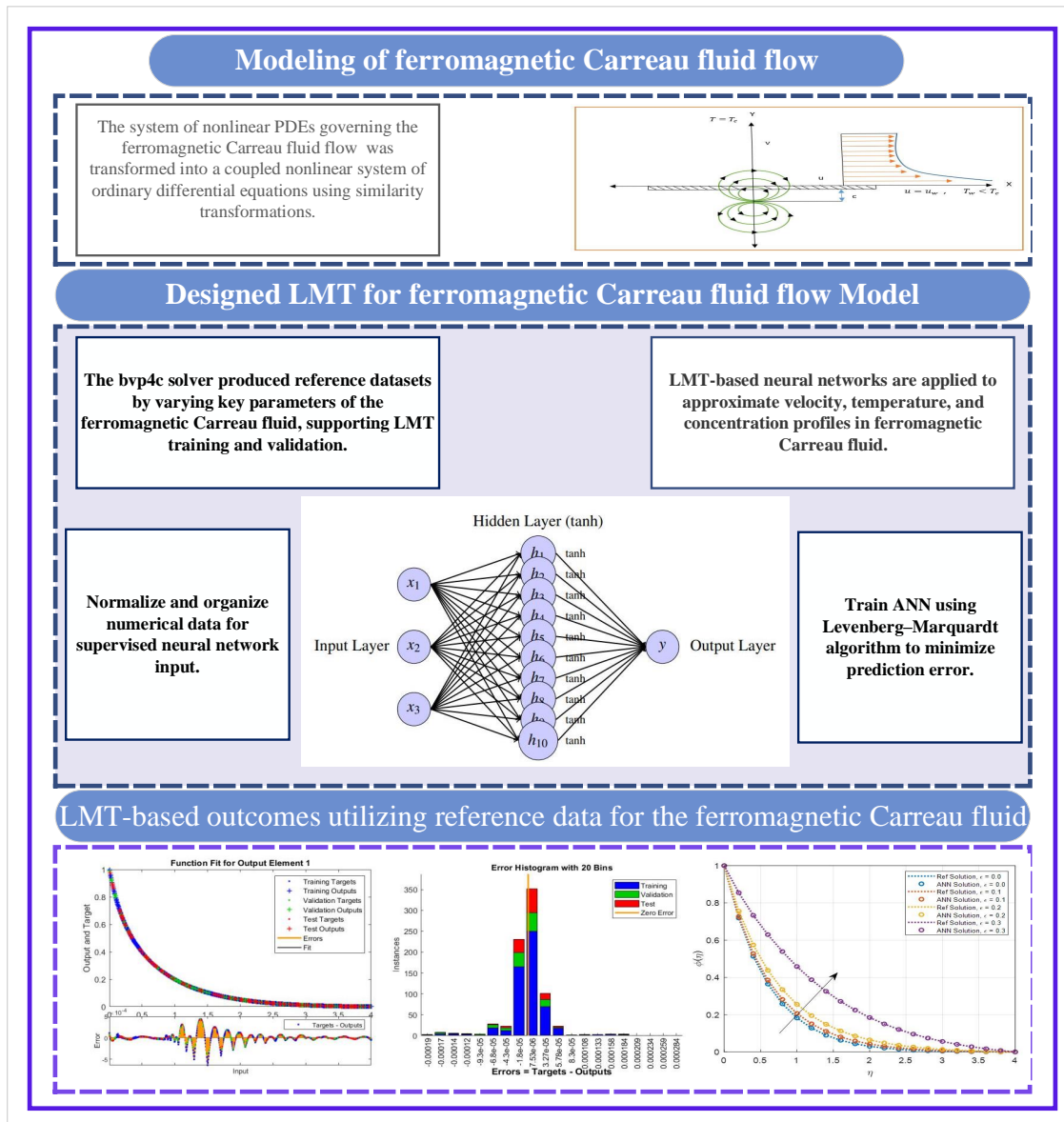
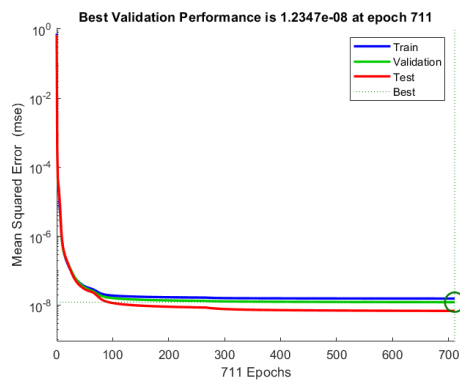
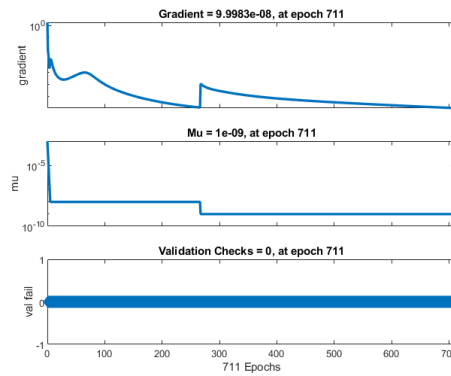


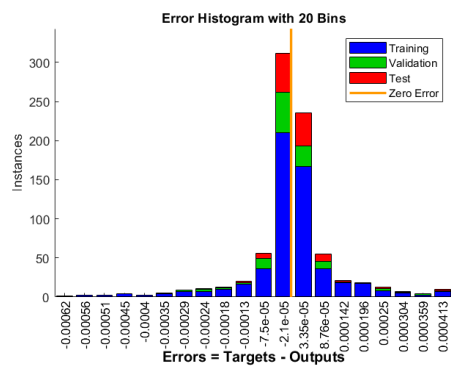
Figure 4: Flow diagram representing the ferromagnetic Carreau fluid model.



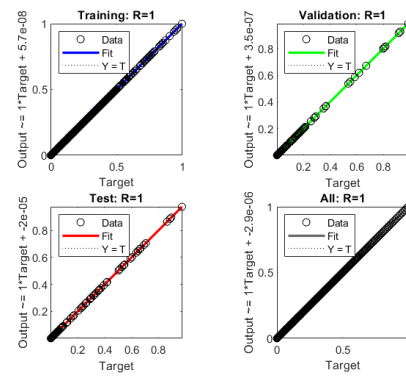
(a) Performance Plot



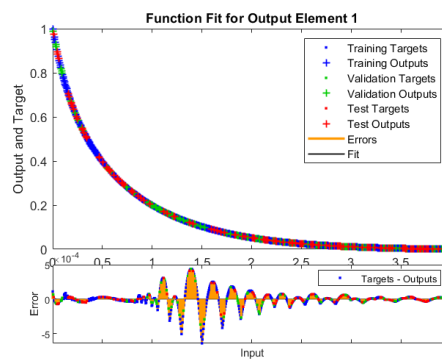
(b) Training State Plot



(c) Error Histogram

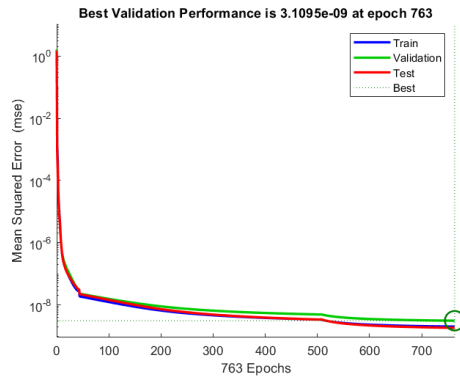


(d) Regression Plot

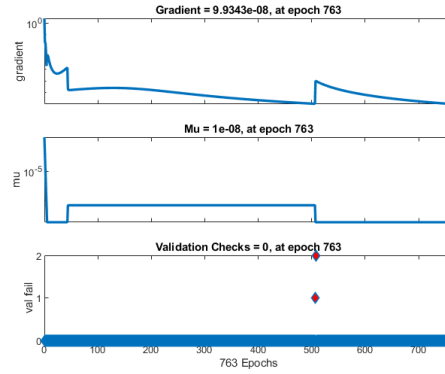


(e) Function fitting graph

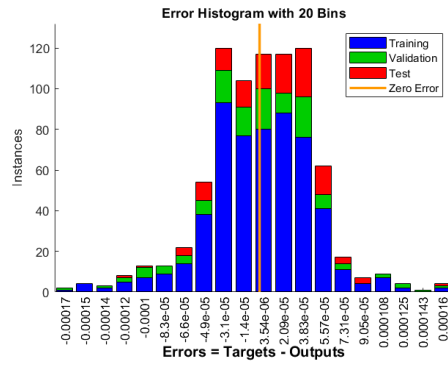
Figure 5: Effect of the melting parameter (B) on LMT-based results



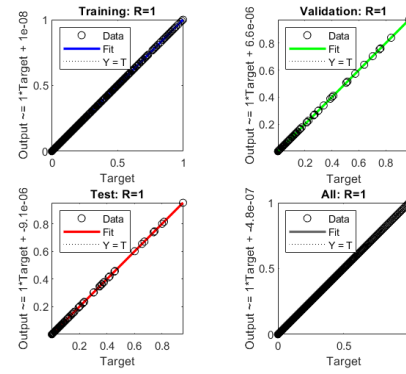
(a) Performance Plot



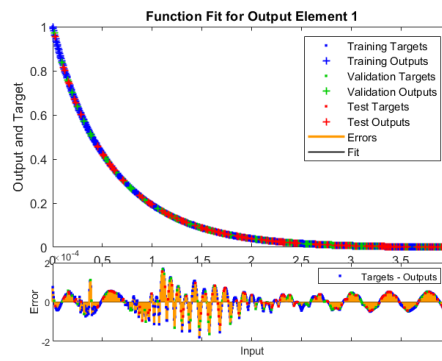
(b) Training State Plot



(c) Error Histogram

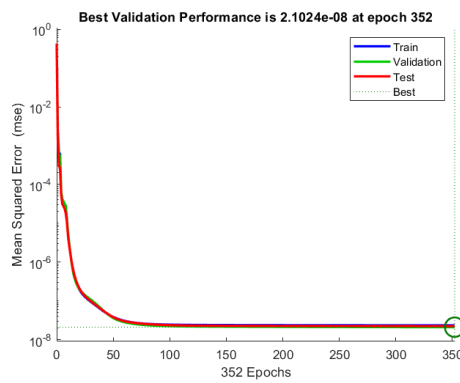


(d) Regression Plot

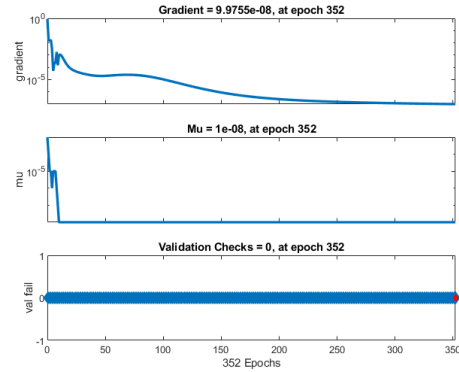


(e) Function fitting graph

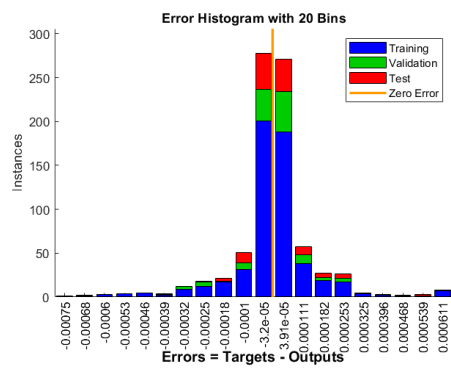
Figure 6: Effect of the ferromagnetic interaction parameter (β) on LMT-based results



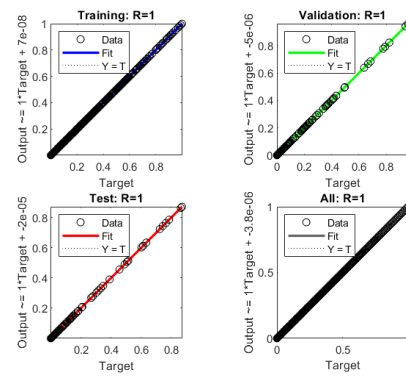
(a) Performance Plot



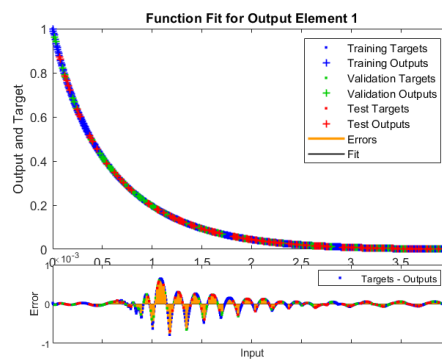
(b) Training State Plot



(c) Error Histogram

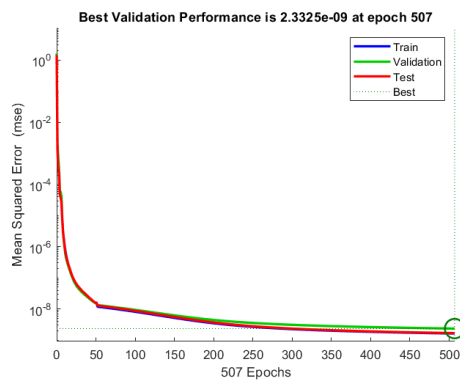


(d) Regression Plot

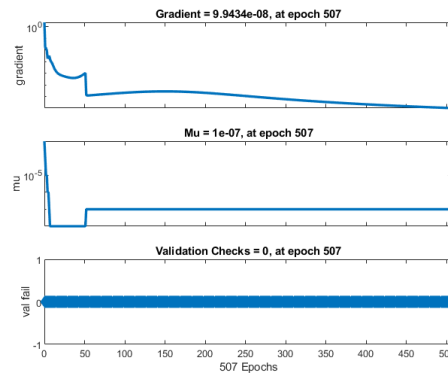


(e) Function fitting graph

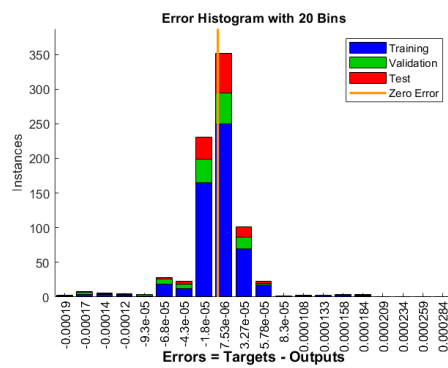
Figure 7: Effect of the Eckert number (Ec) on LMT-based results



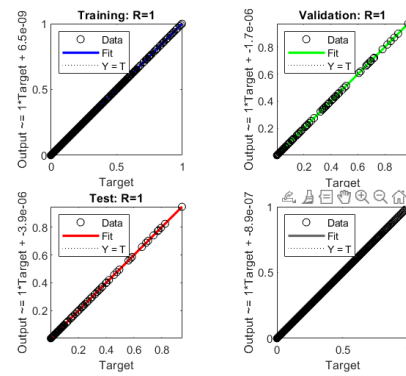
(a) Performance Plot



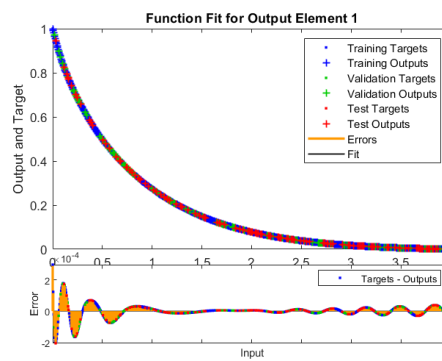
(b) Training State Plot



(c) Error Histogram

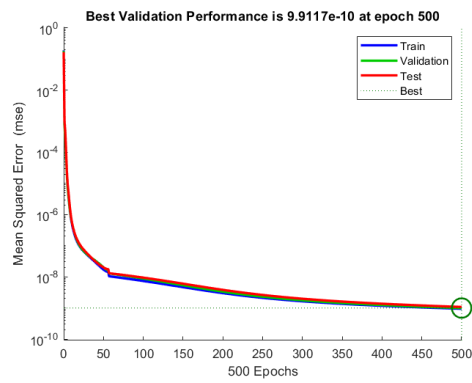


(d) Regression Plot

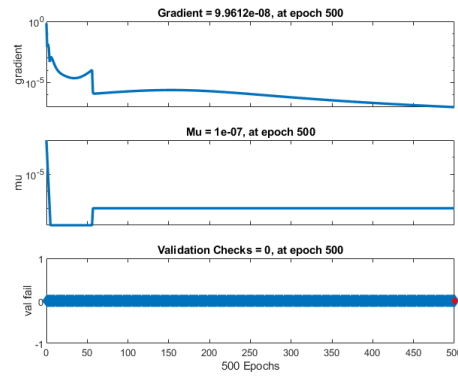


(e) Function fitting graph

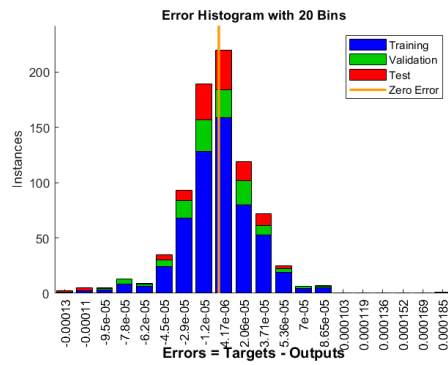
Figure 8: Effect of the Prandtl number (Pr) on LMT-based results



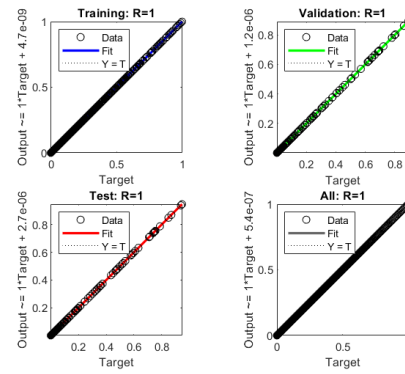
(a) Performance Plot



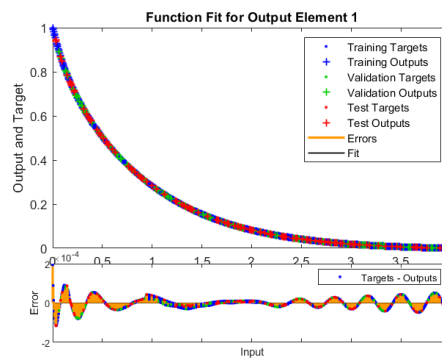
(b) Training State Plot



(c) Error Histogram

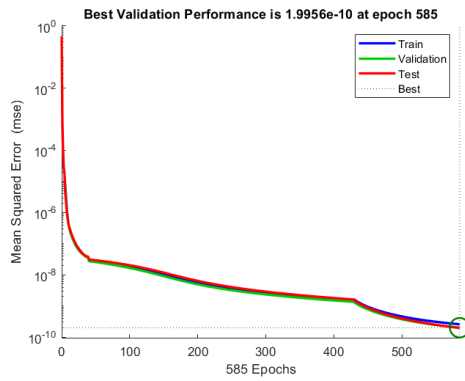


(d) Regression Plot

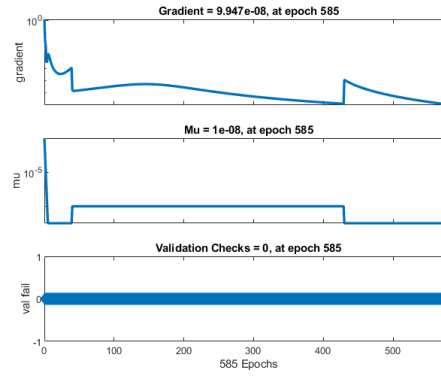


(e) Function fitting graph

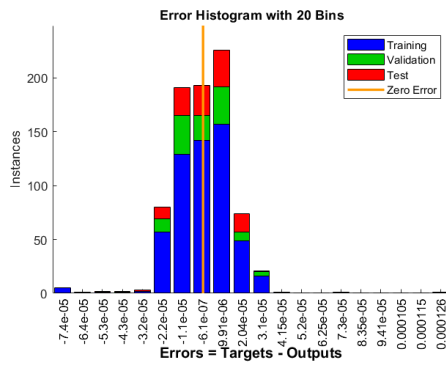
Figure 9: Effect of the Weissenberg number We on LMT-based results.



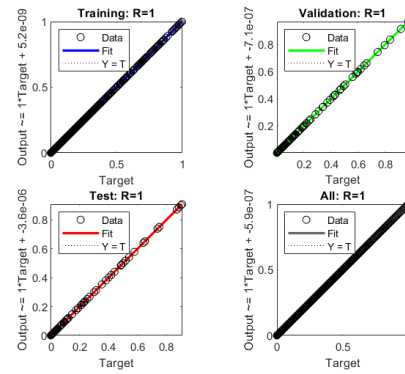
(a) Performance Plot



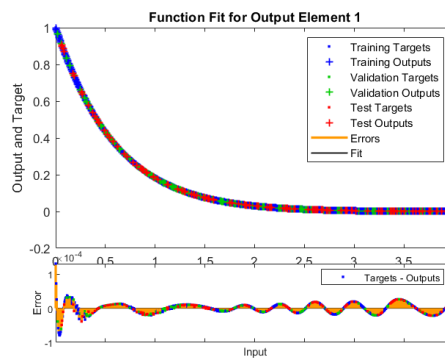
(b) Training State Plot



(c) Error Histogram

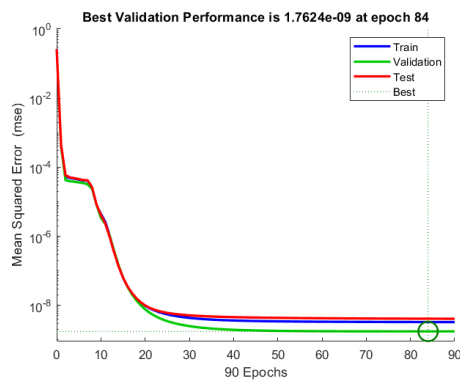


(d) Regression Plot

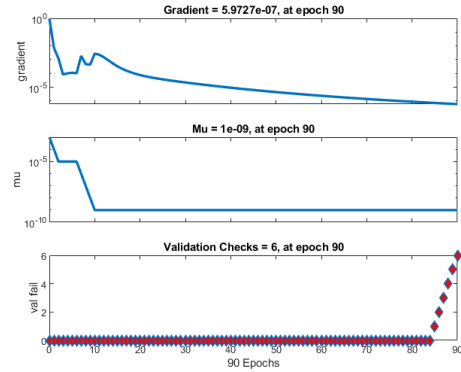


(e) Function fitting graph

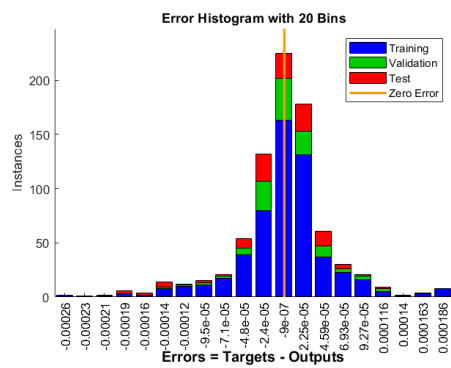
Figure 10: Effect of the Curie temperature ϵ on LMT-based results.



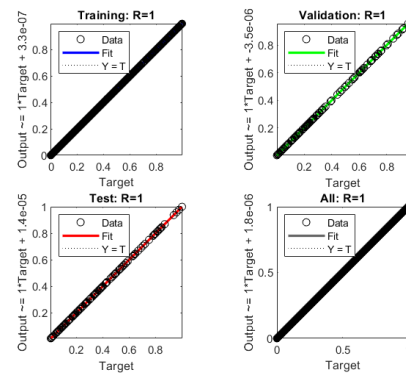
(a) Performance Plot



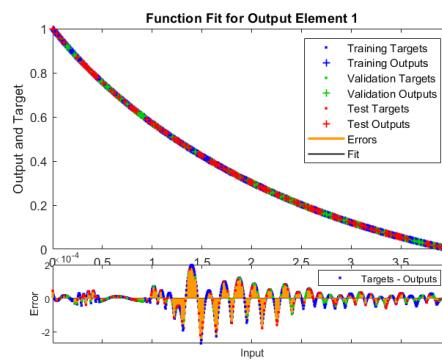
(b) Training State Plot



(c) Error Histogram



(d) Regression Plot



(e) Function fitting graph

Figure 11: Effect of the Schmidt number (Sc) on LMT-based results.

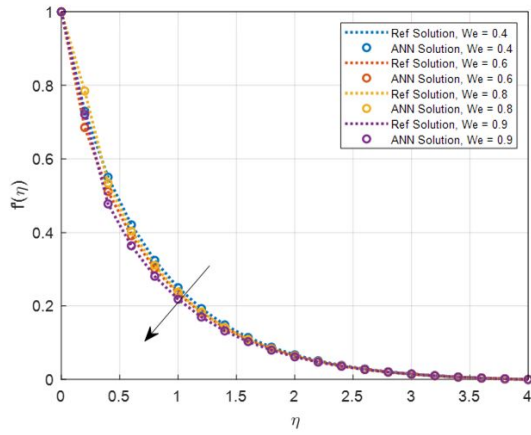


Figure 12: The velocity profile affected by the Weissenberg number (We).

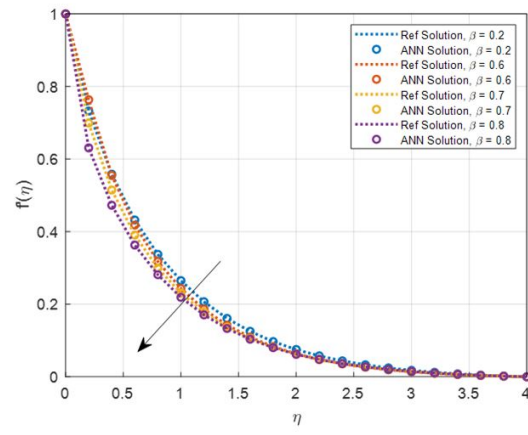


Figure 13: The velocity profile affected by the ferromagnetic interaction parameter (β).

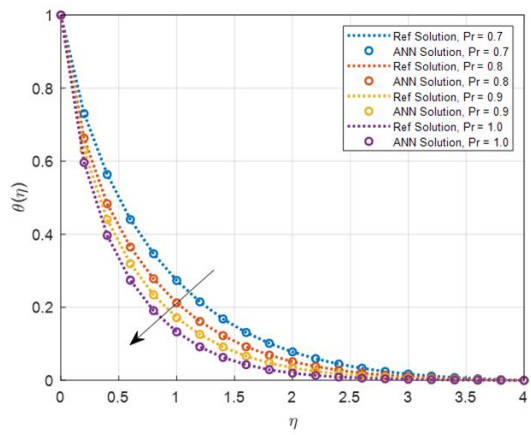


Figure 14: Effect of Weissenberg number (We) on temperature profile.

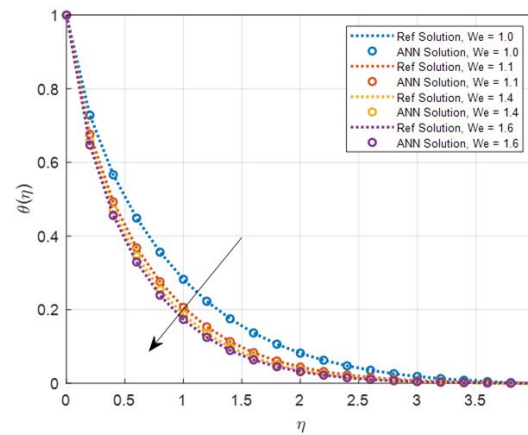


Figure 15: Effect of Prandtl number (Pr) on temperature profile.

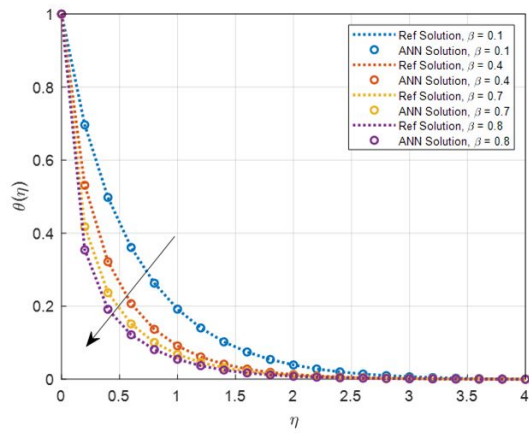


Figure 16: Temperature affected by ferrohydrodynamic interaction parameter (β).

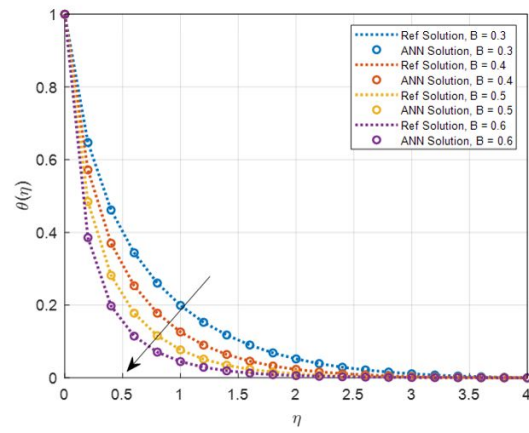


Figure 17: Influence of the melting parameter (B) on temperature profile.

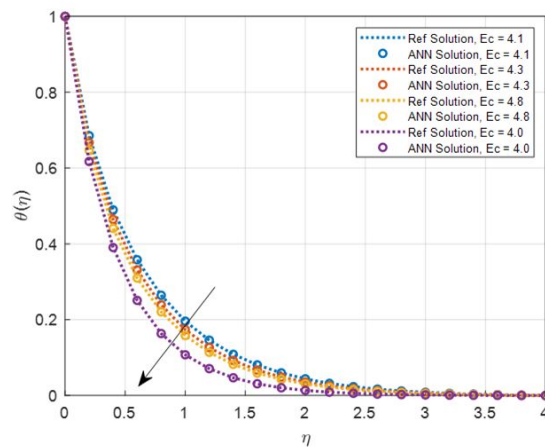
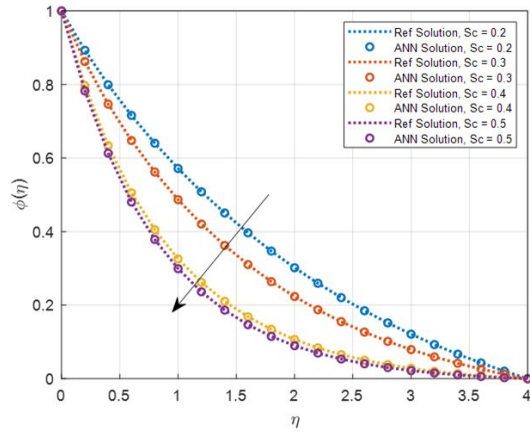
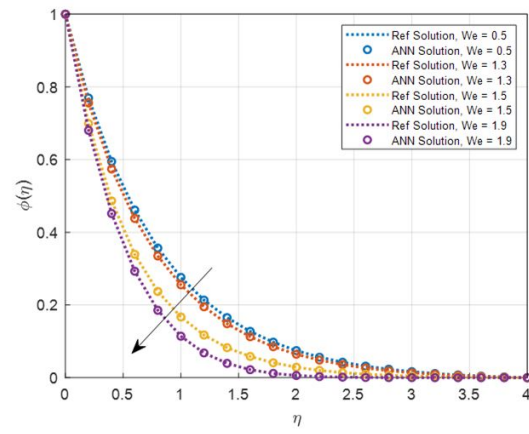
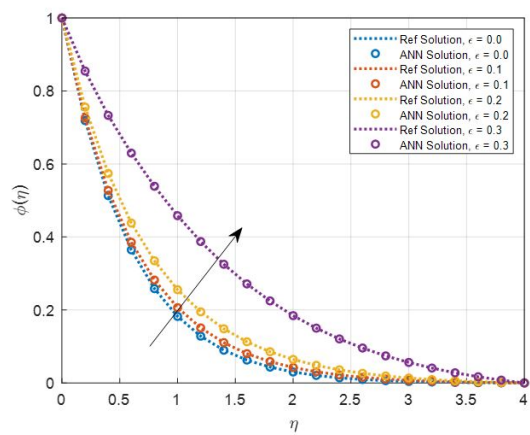
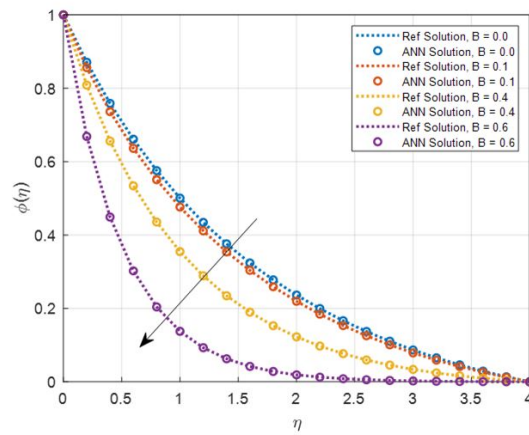


Figure 18: Effect of Eckert number (Ec) on temperature profile.

Figure 19: Effect of Eckert number (Sc) on concentration profile.Figure 20: Effect of Weissenberg number (We) on concentration profile.Figure 21: Influence of Curie temperature (ϵ) on concentration profile.Figure 22: Influence of melting parameter (B) on concentration profile.

5. Conclusion

This study presented a hybrid computational framework combining numerical simulation using MATLAB's `bvp4c` solver and the Levenberg–Marquardt Technique (LMT) to investigate the melting heat transfer and flow behavior of a ferromagnetic Carreau fluid (FCF) influenced by an external magnetic dipole. The effects of key dimensionless parameters, including the melting parameter (B), ferromagnetic interaction parameter (β), Eckert number (Ec), Prandtl number (Pr), Schmidt number (Sc), and dimensionless Curie temperature (ϵ), were comprehensively examined to understand their impact on the flow and thermal characteristics of the system.

- The dataset was divided into 70% for training, 15% for validation, and 15% for testing to ensure robust generalization.
- The LMT-based Artificial Neural Network (ANN) exhibited strong predictive performance, achieving extremely low Mean Squared Error (MSE) values on the order of 10^{-8} to 10^{-10} and high correlation coefficients ($R \approx 1$) across all parameter configurations.
- Optimal convergence occurred at epochs [711, 763, 352, 507, 500, 585, 84], corresponding to MSE values of approximately [1.2347×10^{-8} , 3.1095×10^{-9} , 2.1024×10^{-8} , 2.3325×10^{-9} , 9.9117×10^{-10} , 1.9956×10^{-10} , 1.7624×10^{-9}].
- Error histograms indicated a narrow deviation range [-2.1×10^{-5} , 3.54×10^{-6} , 3.91×10^{-5} , 7.53×10^{-6} , 4.11×10^{-6} , -6.1×10^{-7} , -9×10^{-7}], confirming the network's precision and stability.
- Regression plots and error distributions validated the ANN's reliability, showing that prediction errors were tightly clustered around zero and closely aligned with the reference data.
- Increasing We reduced velocity and concentration due to elastic effects, while temperature responded oppositely for shear-thinning and shear-thickening fluids—indicating energy retention in shear-thinning and suppression in shear-thickening regimes.
- A higher ferromagnetic parameter (β) decreased both velocity and temperature, demonstrating that strong magnetic interactions hinder convective motion and momentum transfer.
- The melting parameter (B) lowered temperature and concentration due to latent heat absorption, weakening energy diffusion and reducing near-wall gradients.
- Larger Pr values thinned the thermal boundary layer as a result of reduced thermal diffusivity, whereas higher Ec values intensified thermal gradients near the wall.
- An increase in Sc weakened solute diffusion, and higher ϵ enhanced near-wall concentration due to diminished magnetic forces near the Curie temperature, reducing solute dispersion.

Overall, the findings confirm the robustness and predictive capability of the ANN–LMT hybrid framework in modeling complex nonlinear ferrohydrodynamic systems involving melting and mass diffusion. The proposed approach offers a computationally efficient and accurate alternative to purely numerical solvers, with significant potential for practical applications in magnetic cooling, materials processing, polymer extrusion, and bioengineering heat transfer systems.

Future studies may focus on unsteady-state and three-dimensional geometries, experimental validation, and the integration of advanced neural architectures such as Physics-Informed Neural Networks (PINNs) to further enhance modeling accuracy, adaptability, and physical consistency.

Table 2: Nomenclature defining symbols, dimensionless parameters, and abbreviations used in the study.

Symbol	Description	Symbol	Description
u, v	Velocity components along x, y	\bar{u}, \bar{v}	Dimensional velocity components
T	Fluid temperature (K)	T_w, T_c, T_∞	Wall, Curie, and ambient temperatures (K)
C	Solute concentration (mol/m ³)	C_w, C_∞	Wall and ambient concentrations (mol/m ³)
ρ	Fluid density (kg/m ³)	μ, ν	Dynamic and kinematic viscosity
k	Thermal conductivity (W/m · K)	c_p	Specific heat at constant pressure (J/kg · K)
μ_0	Magnetic permeability (H/m)	M, H	Magnetization and magnetic field strength
D_B, D_T	Brownian and thermophoretic diffusion coeff.	K	Pyromagnetic coefficient
α_1	Magnetic field constant at source	\bar{c}_1	Distance between dipole and surface
L	Characteristic length (m)	a	Stretching rate constant
\mathbf{D}	Rate of deformation tensor	B_1, D_1	Constants
C_s	Heat capacity of solid surface	λ_1	Latent heat of nanofluid
B	Melting parameter	β	Ferrohydrodynamic interaction parameter
Ec	Eckert number	Pr	Prandtl number
Sc	Schmidt number	We	Weissenberg number
ε	Dimensionless Curie temperature	λ	Viscous dissipation parameter
α	Non-dimensional magnetic dipole distance	n	Power-law index
$f(\eta)$	Dimensionless velocity profile	$\theta(\eta)$	Dimensionless temperature profile
$\phi(\eta)$	Dimensionless concentration profile	η	Similarity variable
$\theta(\eta)$	Dimensionless temperature profile	MSE	Mean Squared Error
ANN	Artificial Neural Network	LMT	Levenberg–Marquardt technique

Table 2 presents a comprehensive overview of all symbols, parameters, and abbreviations used in the analysis, ensuring clarity and consistency throughout the manuscript.

Funding Statement

This study received no particular support from public, corporate, or nonprofit entities.

Declaration of Competing Interest

The authors declare that none of their personal ties or known conflicting financial interests might have seemed to have influenced the work described in this study.

Acknowledgement

The authors are thankful to the University of Management and Technology Lahore Pakistan for facilitating to support this research.

Data Availability

The corresponding author can provide the datasets that were utilized in this work upon reasonable request.

References

- [1] Muhammad Tabrez, Waqar Azeem Khan, Taseer Muhammad, Iftikhar Hussain, and Muhammad Waqas. Significance of thermo-dynamical moment of ferromagnetic nanoparticles and bioconvection analysis for magnetized carreau fluid under the influence of gyrotactic moment of microorganisms. *Tribology International*, 186:108633, 2023.
- [2] Iftikhar Hussain, Waqar Azeem Khan, Muhammad Tabrez, M. Waqas, Talib K. Ibrahim, Taoufik Saidani, M. S. Kausar, Nurnadiah Zamri, Barno Abdullaeva, and Hakim AL Garalleh. A computational framework for carreau nanomaterial induced by stretchy regime considering brownian diffusion, viscous dissipation, ferromagnetism and thermophoresis. *Partial Differential Equations in Applied Mathematics*, 13:101067, 2025.
- [3] Muhammad Tabrez, I. Hussain, W. A. Khan, S. U. Khan, M. Waqas, Rzgar Farooq Rashid, M. I. Anwar, Mohamed Ben Ammar, Nurnadiah Zamri, Ruzimurod Abiyev, et al. Impacts of oxytactic microorganisms and viscous dissipation in carreau nanoliquid featuring ferromagnetic nanoparticles. *Partial Differential Equations in Applied Mathematics*, 13:101027, 2025.
- [4] H. Thameem Basha, R. Sivaraj, A. Subramanyam Reddy, Ali J. Chamkha, and H. M. Baskonus. A numerical study of the ferromagnetic flow of carreau nanofluid over a wedge, plate and stagnation point with a magnetic dipole. *AIMS Mathematics*, 5(5):4197–4220, 2020.
- [5] Syed Amir Ghazi Ali Shah, Ali Hassan, Najah Alsubaie, Abdullah Alhushaybari, Fahad M. Alharbi, Ahmed M. Galal, Diana-Petronela Burduhos-Nergis, and Costica Bejinariu. Convective heat transfer in magneto-hydrodynamic carreau fluid with temperature dependent viscosity and thermal conductivity. *Nanomaterials*, 12(22):4084, 2022.
- [6] Dheia G. Salih Al-Khafajy and Radhwan R. Majeed Mashhadi. The peristaltic flow for carreau fluid through an elastic channel. *Journal of the Mechanical Behavior of Materials*, 32(1):20220257, 2023.
- [7] Sohail Rehman, Ayman Alfaleh, Kallekh Afef, Syed Inayat Ali Shah, et al. Onset about isothermal flow of carreau liquid over converging channel with cattaneo-christov heat and mass fluxes. *Heliyon*, 9(5), 2023.
- [8] N. Kutev, S. Tabakova, and St Radev. Unsteady flow of carreau fluid in a pipe. *Zeitschrift für angewandte Mathematik und Physik*, 72:1–14, 2021.
- [9] Dibyendu Ghosh, Phaojee R. Meena, and Prasanta K. Das. A fully analytical solution of convection in ferrofluids during couette-poiseuille flow subjected to an orthogonal magnetic field. *International Communications in Heat and Mass Transfer*, 130:105793, 2022.

- [10] Iman Al-Obaidi, Hamsa Saleem, and Alaa Hammodat. The effect of a magnetic field on the stability of fluid flow in a porous channel. 2023.
- [11] G. Dharmiah, J. L. Rama Prasad, K. S. Balamurugan, I. Nurhidayat, Unai Fernandez-Gamiz, and Samad Noeiaghdam. Performance of magnetic dipole contribution on ferromagnetic non-newtonian radiative mhd blood flow: An application of biotechnology and medical sciences. *Helvion*, 9(2), 2023.
- [12] A. Hobiny, M. Tabrez, W. A. Khan, and I. Hussain. Numerical analysis of ferromagnetic carreau fluid flow comprising viscos dissipation aspects. *Modern Physics Letters B*, 38(16):2341003, 2024.
- [13] Muhammad Bilal, Ikram Ullah, Mohammad Mahtab Alam, Syed Irfan Shah, and Sayed M. Eldin. Energy transfer in carreau yasuda liquid influenced by engine oil with magnetic dipole using tri-hybrid nanoparticles. *Scientific Reports*, 13(1):5432, 2023.
- [14] G. Thirupathi, K. Govardhan, and G. Narendar. Mhd stagnation point flow of carreau nanofluid over a radially stretching sheet. *International Journal of Nonlinear Analysis and Applications*, 14(1):1093–1109, 2023.
- [15] S. K. Asha and Joonabi Beleri. Peristaltic flow of carreau nanofluid in presence of joule heat effect in an inclined asymmetric channel by multi-step differential transformation method. *World Scientific News*, 164:44–63, 2022.
- [16] Muhammad Rooman, Zahir Shah, Ebenezer Bonyah, Muhammad Asif Jan, and Wejdan Deebani. Mathematical modeling of carreau fluid flow and heat transfer characteristics in the renal tubule. *Journal of Mathematics*, 2022(1):2517933, 2022.
- [17] Kenneth Levenberg. A method for the solution of certain non-linear problems in least squares. *Quarterly of Applied Mathematics*, 2(2):164–168, 1944.
- [18] Donald W. Marquardt. An algorithm for least-squares estimation of nonlinear parameters. *Journal of the Society for Industrial and Applied Mathematics*, 11(2):431–441, 1963.
- [19] Martin T. Hagan and Mohammad B. Menhaj. Training feedforward networks with the marquardt algorithm. *IEEE Transactions on Neural Networks*, 5(6):989–993, 1994.
- [20] Jorge J. Moré. The levenberg-marquardt algorithm: Implementation and theory. pages 105–116, 1978.
- [21] Chih-Chieh Huang and Chin-Hsiung Loh. Nonlinear identification of dynamic systems using neural networks. *Computer-Aided Civil and Infrastructure Engineering*, 16(1):28–41, 2001.
- [22] Nafisa A. Albasheir, Zahoor Shah, Muhammad Asif Zahoor Raja, Amel A. Touati, Mohammed M. A. Almazah, Maryam Jawaid, and M. Waqas. Ai-powered levenberg-marquardt neural networks for implementation of novel flux conditions in carreau nanomaterial stagnation-point flow considering magnetic field and heat source effects. *Measurement*, 243:116304, 2025.
- [23] Khalil Ur Rehman, Wasfi Shatanawi, and Abdul Rahman Mohd Kasim. On heat transfer in carreau fluid flow with thermal slip: an artificial intelligence (ai) based decisions integrated with lie symmetry. *International Journal of Heat and Fluid Flow*, 107:109409, 2024.

- [24] Ahmed Jan, Muhammad Mushtaq, Muhammad Imran Khan, and Umer Farooq. Integrated artificial intelligence and non-similar analysis for forced convection of radially magnetized ternary hybrid nanofluid of carreau-yasuda fluid model over a curved stretching surface. *International Journal for Numerical Methods in Fluids*, 96(12):1864–1882, 2024.
- [25] Adil Darvesh, Fethi Mohamed Maiz, Basma Souayeh, Luis Jaime Collantes Santisteban, Hakim AL Garalleh, Afnan Al Agha, Lucerito Katherine Ortiz García, and Nicole Anarella Sánchez-Miranda. Ann-based two hidden layers computational procedure for analysis of heat transport dynamics in polymer-based trihybrid carreau nanofluid flow over needle geometry. *Hybrid Advances*, page 100396, 2025.
- [26] Khalil Ur Rehman, Wasfi Shatanawi, and Andaç Çolak. Neural networking-based analysis of heat transfer in mhd thermally slip carreau fluid flow with heat generation. *Case Studies in Thermal Engineering*, 54, 2024.
- [27] Aqsa Zafar Abbasi, Mamoon Aamir, Mariyam Sattar, Nermeen Abdullah, Tarek Salem Abdennaji, Badr M. Alshammri, and Lioua Kolsi. Modelling and prediction of 3d carreau fluid behaviour using machine learning for cattaneo christov double diffusion with variable conductivity. *Case Studies in Thermal Engineering*, page 106302, 2025.
- [28] Omar Salah H. Alhamdi and N. Ameer Ahammad. Numerical computation of bio-convective carreau blood nanofluid flow across three geometries with nonlinear thermal radiation: heat transfer optimization via supervised machine learning. *The European Physical Journal Special Topics*, pages 1–27, 2024.
- [29] Muhammad Shoaib, Kottakkaran Sooppy Nisar, Muhammad Asif Zahoor Raja, Aqsa Zafar Abbasi, Rafia Tabassum, and Ayesha Rafiq. Stochastic numerical computing for hydro-magnetic flow of carreau-nanofluid model. *Waves in Random and Complex Media*, pages 1–20, 2023.
- [30] Mohammad Alqudah, Syed Zahir Hussain Shah, Muhammad Bilal Riaz, Hamiden Abd El-Wahed Khalifa, Ali Akgül, and Assad Ayub. Neural network architecture to optimize the nanoscale thermal transport of ternary magnetized carreau nanofluid over 3d wedge. *Results in Physics*, 59:107616, 2024.
- [31] P. Priyadharshini, M. Vanitha Archana, Nehad Ali Shah, and Mansoor H. Alshehri. Ternary hybrid nanofluid flow emerging on a symmetrically stretching sheet optimization with machine learning prediction scheme. *Symmetry*, 15(6):1225, 2023.
- [32] P. Priyadharshini, M. Vanitha Archana, N. Ameer Ahammad, Chakravarthula S. K. Raju, Se-jin Yook, and Nehad Ali Shah. Gradient descent machine learning regression for mhd flow: Metallurgy process. *International Communications in Heat and Mass Transfer*, 138:106307, 2022.
- [33] Maddina Dinesh Kumar, C. S. K. Raju, Kiran Sajjan, Gurram Dharmaiah, Nehad Ali Shah, and Se-Jin Yook. Deep neural network-based prediction and computational fluid dynamics analysis of convective heat transfer in dusty fluid flow over heated surface. *Physics of Fluids*, 37(2), 2025.
- [34] Maddina Dinesh Kumar, C. S. K. Raju, Nehad Ali Shah, Se-Jin Yook, and Dharmaiah Gurram. Support vector machine learning classification of heat transfer rate in tri-

- hybrid nanofluid over a 3d stretching surface with suction effects for water at 10° c and 50° c. *Alexandria Engineering Journal*, 118:556–578, 2025.
- [35] Rupa Baithalu, S. R. Mishra, Subhajit Panda, and Nehad Ali Shah. Forced convective micropolar nanofluidic transportation with cattaneo-christov heat and mass flux model: Levenberg-marquardt backpropagation neural network approach. *Engineering Applications of Artificial Intelligence*, 154:110947, 2025.
- [36] Assad Ayub, Zahoor Iqbal, Syed Zahir Hussain Shah, Fathia M. Al Samman, Hafiz Abdul Wahab, Mhassen E. E. Dalam, and Ameni Gargouri. Neural intelligent approach for heat transfer applications of trihybrid cross bio-nanofluid over wedge geometry. *Modern Physics Letters B*, 39(10):2450439, 2025.
- [37] Atifa Asghar, Rukhsar Ikram, Amir Khan, Mohsan Hassan, and Aeshah A. Raezah. Applications of artificial neural network to solve the nonlinear cassava mosaic disease model. *The European Physical Journal Plus*, 139(11):1012, 2024.
- [38] Mohsan Hassan, Syed Tauseef Mohyud-Din, and Muhammad Ramzan. Study of heat transfer and entropy generation in ferrofluid under low oscillating magnetic field. *Indian Journal of Physics*, pages 1–10, 2018.
- [39] Muhammad Rizwan, Mohsan Hassan, Oluwole Daniel Makinde, Muhammad Mubashir Bhatti, and Marin Marin. Rheological modeling of metallic oxide nanoparticles containing non-newtonian nanofluids and potential investigation of heat and mass flow characteristics. *Nanomaterials*, 12(7):1237, 2022.
- [40] Khalid Arif, Syed Tauseef Saeed, Muhammad Naeem Aslam, Jihad Younis, Arshad Riaz, and Salman Saleem. Modelling cross-diffusion in mhd williamson nanofluid flow over a nonlinear stretching surface via morlet wavelet neural networks. *Scientific Reports*, 15(1):27287, 2025.
- [41] Ibrahim Alraddadi, Assad Ayub, Syed Modassir Hussain, Umair Khan, Syed Zahir Hussain Shah, and Ahmed M. Hassan. The significance of ternary hybrid cross bio-nanofluid model in expanding/contracting cylinder with inclined magnetic field. *Frontiers in Materials*, 10:1242085, 2023.
- [42] Syed Zahir Hussain Shah, Zulqurnain Sabir, Assad Ayub, Amjid Rashid, R. Sadat, and Mohamed R. Ali. An efficient numerical scheme for solving the melting transportation of energy with time dependent carreau nanofluid. *South African Journal of Chemical Engineering*, 47:345–356, 2024.
- [43] Syed Zahir Hussain Shah, Assad Ayub, Saira Bhatti, Umair Khan, Anuar Ishak, El-Sayed M. Sherif, and Ioan Pop. Aspects of inclined magnetohydrodynamics and heat transfer in a non-newtonian tri-hybrid bio-nanofluid flow past a wedge-shaped artery utilizing artificial neural network scheme. *ZAMM-Journal of Applied Mathematics and Mechanics/Zeitschrift für Angewandte Mathematik und Mechanik*, 104(12):e202400278, 2024.
- [44] Mehari Fentahun Endalew and Subharthi Sarkar. Numerical exploration of forced convection hydromagnetic hyperbolic tangent nanofluid flow over a permeable wedge with melting heat transfer. *Scientific Reports*, 13(1):3515, 2023.
- [45] L. R. Titus and A. Abraham. Flow of ferrofluid over an inclined stretching sheet in the presence. In *Transactions on Engineering Technologies: World Congress on*

Engineering, page 41, 2018.